Energy & Environmental Science

PAPER

View Article Online
View Journal | View Issue

Cite this: *Energy Environ. Sci.*, 2015, **8**, 303

A high efficiency solution processed polymer inverted triple-junction solar cell exhibiting a power conversion efficiency of 11.83%†

Abd. Rashid bin Mohd Yusoff,*[a] Dongcheon Kim,[a] Hyeong Pil Kim,[a] Fabio Kurt Shneider,[b] Wilson Jose da Silva[b] and Jin Jang[a]

Received 25th September 2014
Accepted 30th October 2014

DOI: 10.1039/c4ee03048f

www.rsc.org/ees

High efficiency, solution-deposited polymer inverted double- and triple-junction solar cells are demonstrated. The devices are composed of three distinctive photosensitive materials in three distinct subcells, with minimal absorption spectral overlap, and with a bandgap ranging from 1.3 eV to 1.82 eV. A transparent hybrid inorganic organic mixture was introduced as an interconnecting layer to optically and physically connect the subcells. Accordingly, a power conversion efficiency of 10.39% was attained for the double-junction cell and a record high of 11.83% was obtained for the triple-junction cell.

Broader context

Today, a change in people's attitudes towards a green lifestyle has led to a shift in their approach towards life, whereby they are trying to reduce their impact on the environment. Hence, various methods have been used to reduce the use of fossil fuels, such as wind, hydro, tidal, wave, geothermal, biomass, wood, and solar energies. Among these clean technologies, solar energy is considered as very appealing owing to various aspects, including cost, accessibility, and an inexhaustible source. Polymer solar cells, in particular, are capable of converting sunlight into electricity. Multi-junction solar cells, where more than two single-junction solar cells vertically stacked up are connected in series by a robust and transparent interconnecting layer, have demonstrated not only higher performance but have also overcome the two major issues of single-junction solar cells. These issues include the thermalization of excited carriers and the transmission of unabsorbed photons. In this study, a novel all solution processed multi-junction structure was employed to improve the light absorption, and has led us to fabricate highly efficient multi-junction polymer solar cells.

Polymer solar cells (PSCs) offer great advantages as a possible future energy source because they are light-weight, cost-effective, and mechanically flexible.[1–5] A significant amount of focus has been recently shifted towards the development of highly efficient PSCs. This includes developing novel donor materials,[6–15] optimizing the surface topography of the photosensitive layer,[5,16,17] and interface engineering.[18–25] Accordingly, Yang *et al.* documented a record-high power conversion efficiency (PCE) of 10.6%.[26] Apart from the swift advancement in the material design and in the photosensitive layer engineering, PSCs suffer from two major losses: (i) the thermalization of excited carriers, and (ii) the transmission of unabsorbed photons. The first loss occurs when photons with a higher energy than the energy bandgap of the polymer or organic semiconductor are absorbed. This is a common loss in solar-cell conversion and the development of such an ultrafast platform could possibly enable operation at high temperatures. This would enable a better use of free energy in the photons over the entire visible spectrum by up to 40%. The second loss is due to the transmission of photons having a relatively lower energy through the cell from being absorbed than the bandgap energy. In this case, the thickness of the donor material should be equal to the absorption length of the photon of energy equal to the bandgap energy.

Thus, a so-called tandem or multi-junction architecture has been the centre of attraction for researchers, due to their higher overall PCE.[3,27–36] Tandem PSCs are fabricated by vertically piling multiple single-junction solar cells that are physically connected by an interconnecting layer (ICL) with a broader absorption band. Hence, it is imperative to design low bandgap absorption donors that can extend the light absorption edge into the near-infra-red (NIR) regime to capture more photons, and at the same time maintain a high hole-mobility for efficient charge carrier transport. In general, in series connected tandem solar cells, the open circuit voltage (V_{oc}) is equal to the summation of the front and bottom subcells. However, in parallel connected tandem solar cells, the short circuit current density (J_{sc}) is equal to the summation of the J_{sc} obtained in the front and bottom subcells. Recently, Heliatek, one of the

[a]*Department of Information, Display and Advanced Display Research Center, Kyung Hee University, Dongdaemun-ku, Seoul 130-171, Republic of Korea. E-mail: jjang@khu.ac.kr; Fax: +82 2 961 0270; Tel: +82 2 961 0270*

[b]*Universidade Tecnologica Federal do Parana, GPGEI – Av. Sete de Setembro, 3165 – CEP 80230-901, Curitiba, Parana, Brazil. E-mail: wjsilva2000@yahoo.com.br; Tel: +55 41 33104691*

† Electronic supplementary information (ESI) available. See DOI: 10.1039/c4ee03048f

leading research institutes, announced 12% efficient tandem small molecules.[37] Rapid progress on multi-junction PSCs indicates there is considerable potential for further improvement, for example, Janssen *et al.* were able to demonstrate two different triple-junction PSCs along with V_{oc} of 2.33 V and 2.09 V.[38,39] However, due to the identical donor layers in the middle and bottom subcells, the generated photocurrents of both the triple-junction devices were limited by the charge carrier generation of the subcells. They both had the same spectral response, which led to unsatisfactory performance.

To date, triple-junction PSCs have attracted significant interest, where Forrest *et al.*[40] demonstrated vacuum-deposited small molecule triple-junction PSCs. In their reported work, the tandem structure used an orange-to-near infrared (NIR) and an ultraviolet-to-yellow small molecule as their front and bottom subcells. This yielded a PCE of 10% with a J_{sc} of 9.9 mA cm^{-2}, a V_{oc} of 1.72 V, and a fill factor (FF) of 59%. Further improvements were demonstrated in the triple-junction architecture, when NIR was sandwiched between the absorbing donors and the yellow small molecules were the middle subcell. They also recorded astonishing enhancements in device performance, registering a high V_{oc} of 2.58 V, J_{sc} of 7.3 mA cm^{-2}, and a PCE of 11.1%. However, a major shortcoming of this work was the fact that the FF is only 59%.

Very recently, the bandgap engineering of subcells in triple-junction PSCs has resulted in 11.55% efficiency triple-junction PSCs with a V_{oc} of 2.28 V, a J_{sc} of 7.63 mA cm^{-2}, and a FF of 66.39%.[41] In this study, they proposed such arrangements for high efficiency triple-junction PSCs, featuring wide, medium, and low bandgaps as the front, middle, and bottom subcells, respectively. Advances in the design and bandgap arrangement led to a reduced carrier recombination and voltage loss. This arrangement is quite similar to the one used in the III–V multi-junction solar cell. The desirable approach is first to have the sunlight project onto the wide bandgap subcell, and then to continue progressively onto the low bandgap subcell. This arrangement utilizes the subcell functions of low-pass photon energy filters, transmitting only the sub bandgap light. On that account, photons with $hv > E_{g3}$ get absorbed by the E_{g3} subcell, and the photons with $E_{g2} < hv < E_{g3}$ get absorbed by the E_{g2} subcell. The subcells themselves serve as optical elements to distribute the spectrum to the appropriate junctions for the multi-junction photoconversion. The bandgap must decrease from the front to the bottom of the stack as, wide bandgap (1.85–2 eV) > medium bandgap (1.2–1.4 eV) > low bandgap (0.7–1 eV).[42] This is done in order to absorb and convert the photons that have energies greater than the bandgap of that layer but less than the bandgap of the higher layer. Hence, bandgaps are not the only aspect needed in developing highly efficient multi-junction solar cells, the series connected multi-junction solar cells are the ones that make current matching a desirable characteristic. The output photocurrent of the multi-junction solar cell is restrained by the lowest current generated from the wide bandgap front subcell. In this case, the current through each of the subcells is restricted to having a similar value. The photocurrent is proportional to the number of incident photons exceeding the material and absorption constant of the photosensitive material. Accordingly, a layer must be made thinner if the photons exceeding the bandgap are in excess. Moreover, a layer with a low absorption constant must be made thicker, because normally, a photon must pass through more of the material before being absorbed.

Therefore, in this work we make full use of bandgap engineering to demonstrate fully solution-processed inverted double-junction and inverted triple-junction PSCs. In the tandem architecture, the front subcell close to the transparent conducting electrode indium tin oxide (ITO) consists of the wide bandgap absorbing donor, poly[(4,4′-bis(3-ethyl-hexyl)-dithieno[3,2-*b*′′:3′-*d*]silole)-2,6-diyl-*alt*-(2,5-(3-(2-ethyl-hexyl)thiophen-2-yl)thiazolo[5,4-*d*]thiazole] (PSEHTT)[43] blended with indene-C_{60} bisadduct ($IC_{60}BA$)[44] and is paired with a medium bandgap absorbing donor, thieno[3,4-*b*]thiophene/benzodithiophene (PTB7),[45] and mixed with [6,6]phenyl-C_{71}-butyric acid methyl ester ($PC_{71}BM$)[46] (Fig. 1a). The inverted tandem PSCs broadly cover the solar spectrum from $\lambda = 300$ to 800 nm, achieving a V_{oc} of 1.54 ± 0.01 V, a J_{sc} of 10.30 ± 0.01 mA cm^{-2} (spectral mismatch factor $M = 0.97 \pm 0.03$), and a FF of 65.47 ± 0.02%. This corresponds to a PCE of 10.39 ± 0.03% under AM 1.5G illumination (25 °C, 100 mW cm^{-2}).

To further boost the efficiency of the inverted tandem PSC, it is possible to stack an additional low bandgap third subcell, forming an inverted triple-junction PSC with a 1 + 1 + 1 configuration. The driving force behind having an extra subcell is that in the tandem cell, the generated photocurrent is restricted by the wide bandgap front subcell. Therefore, we anticipate that the low bandgap bottom subcell will supply the remaining photocurrent that will not be used in the top double-PSCs. By using this technique, along with careful bandgap engineering, our inverted triple-junction PSC demonstrates a PCE of 11.83 ± 0.02%, exceeding the previous record set by Yang *et al.*[41] along with a V_{oc} of 2.24 V ± 0.01 V, a FF of 67.52 ± 0.03%, and a J_{sc} of 7.83 ± 0.03 mA cm^{-2} ($M = 1.01 \pm 0.02$), suggesting huge potential for multi-junction PSCs research.

The refractive indices (n) and extinction coefficients (k) of the two absorbing donors, PSEHTT:$IC_{60}BA$ (left) and PTB7:$PC_{71}BM$ (right) are shown in Fig. 1b, respectively. For our inverted tandem PSCs, we chose donor materials that provide a relatively high V_{oc} with fullerene acceptors. The front subcell is a blend of the PSEHTT ($E_{g1} = 1.82$ eV) as the donor and $IC_{60}BA$ as the acceptor, while the bottom subcell consists of a blend of PTB7 ($E_{g2} = 1.6$ eV) and $PC_{71}BM$.

Fig. 1c illustrates the schematic architecture of the complete inverted tandem PSCs. The wide bandgap of PSEHTT:$IC_{60}BA$ is physically connected with the medium bandgap PTB7:$PC_{71}BM$ *via* ICL, which consists of lithium zinc oxide (LZO)[23] as the electron transport layer (ETL) and pH-neutral PEDOT:PSS as the hole transport layer (HTL).[23] The C_{60}-self-assembled monolayer (SAM) is used to modify the interface of the metal oxide/active layer. To determine the optimal thickness of the front and bottom subcells, optical and electrical modelling were performed.[29] Throughout this study, we successfully performed systematic optimization experiments to create the most efficient inverted tandem PSCs.

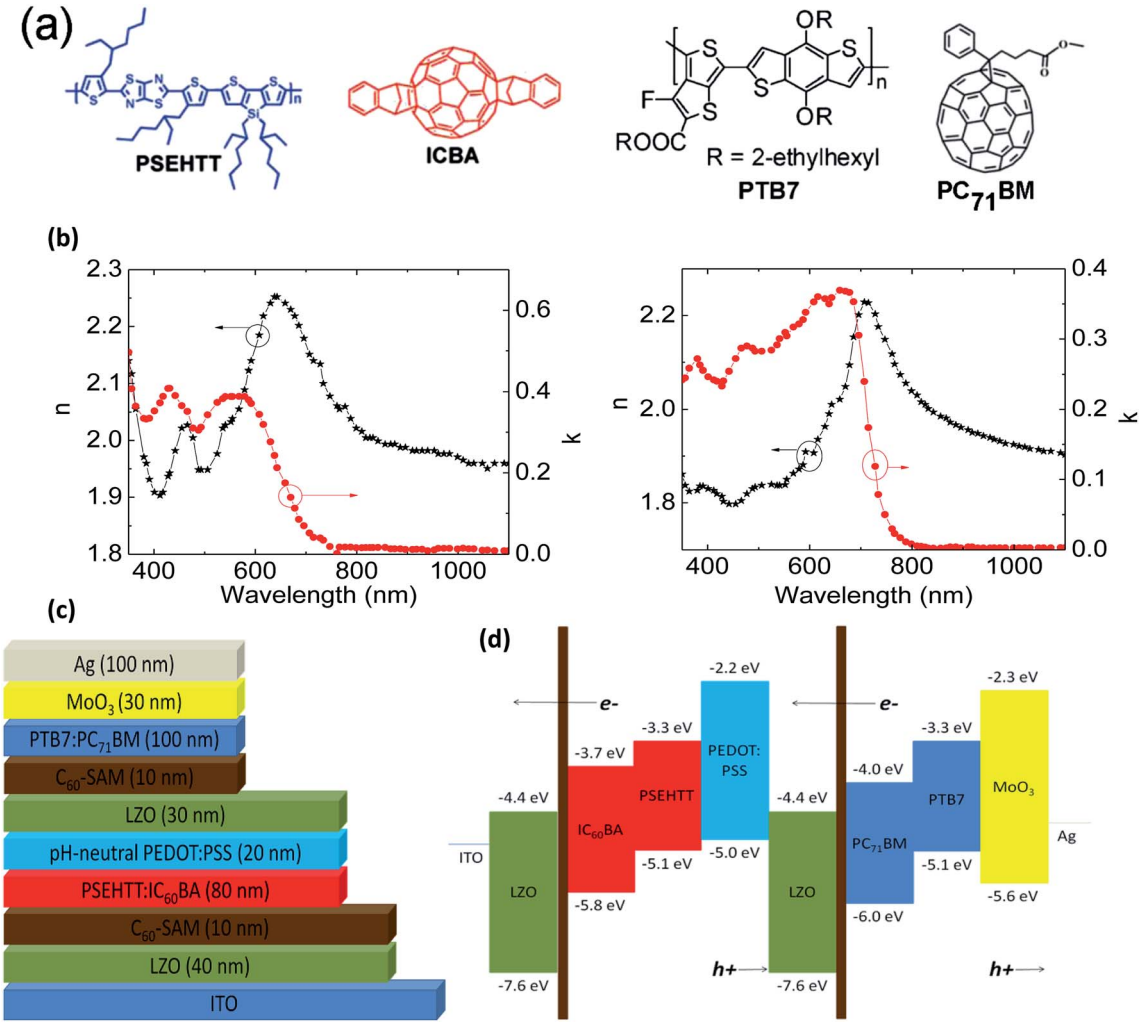

Fig. 1 (a) Chemical structures of the polymers and fullerenes used in the polymer inverted tandem cell. (b) Optical parameters *n* and *k* for PSEHTT:$IC_{60}BA$ (left), and PTB7:$PC_{71}BM$ (right). (c) Polymer inverted tandem cell: ITO/LZO/C_{60}-SAM/PSEHTT:$IC_{60}BA$/pH-neutral PEDOT:PSS/LZO/C_{60}-SAM/PTB7:$PC_{71}BM$/MoO_3/Ag. (d) Proposed energy level of the polymer inverted tandem cell.

In determining the ideal bulk heterojunction (BHJ) thickness that optimizes the photocurrent in the inverted tandem PSC, two independent optimizations were performed. We changed the spin coating speed from 500 rpm to 1050 rpm for the PSEHTT:$IC_{60}BA$ front and PTB7:$PC_{71}BM$ bottom subcells. First, we found the thickness of the photosensitive material of the PSEHTT:$IC_{60}BA$ front subcell varied. However, the thickness of the photosensitive material of the PTB7:$PC_{71}BM$ bottom subcell maintained a value of 100 nm (500 rpm). All the data in Table 1 demonstrate the photovoltaic performance variations of the single-junction PSCs, and Fig. 2a exhibits their respective *J*–*V* characteristics. As anticipated, the device performance

Table 1 Device performance of PSEHTT:$IC_{60}BA$-based single junction solar cells with different photosensitive thicknesses and different ETLs. The values in Table 1 are the average of 47 devices

PSEHTT:$IC_{60}BA$ thickness (nm)	ETL	J_{sc} (mA cm^{-2})	V_{oc} (V)	FF (%)	PCE (%)	*M*
70	LZO	10.10 ± 0.01	0.94 ± 0.01	66.55 ± 0.02	6.32 ± 0.01	1.03 ± 0.02
80	LZO	10.65 ± 0.02	0.94 ± 0.01	65.84 ± 0.03	6.59 ± 0.01	1.08 ± 0.02
90	LZO	10.25 ± 0.01	0.94 ± 0.01	65.08 ± 0.02	6.27 ± 0.02	0.97 ± 0.01
100	LZO	9.55 ± 0.01	0.94 ± 0.01	63.86 ± 0.02	5.73 ± 0.01	0.95 ± 0.03
80	ZnO	9.87 ± 0.03	0.91 ± 0.01	61.11 ± 0.01	5.46 ± 0.02	1.06 ± 0.02
90	TiO_2	10.21 ± 0.02	0.91 ± 0.01	62.02 ± 0.01	5.76 ± 0.01	1.00 ± 0.02

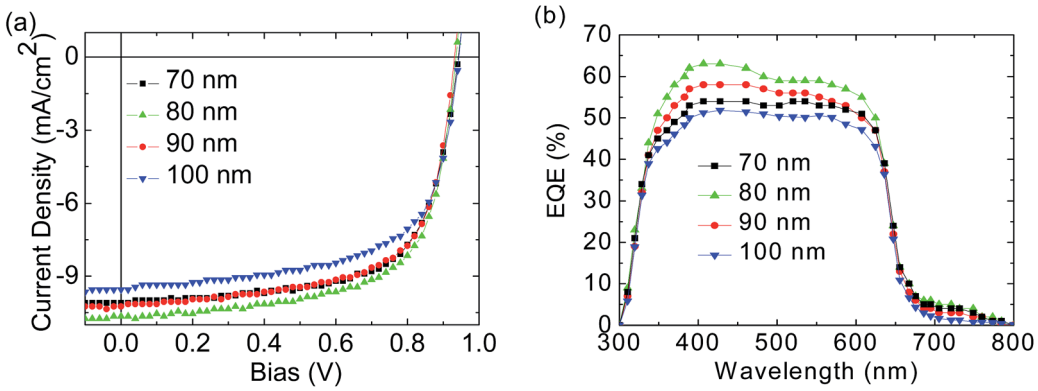

Fig. 2 PSEHTT:$IC_{60}BA$-based single junction solar cells performance with different photosensitive thicknesses with LZO ETL under AM 1.5G illumination (25 °C, 100 mW cm^{-2}). (a) *J–V* curves. (b) External quantum efficiency.

became poorer as the BHJ layer got thinner (70 nm), yielding less absorption and less J_{sc} (10.10 ± 0.01 mA cm^{-2}). The J_{sc} of the device was enhanced to 10.25 ± 0.01 from 10.10 ± 0.01 mA cm^{-2}, as the thickness of the BHJ layer increased to 90 nm from 70 nm. The maximum J_{sc} of 10.65 ± 0.02 mA cm^{-2} (M = 1.08 ± 0.02) was obtained from the 80 nm device. The FF decreased with the increase in thickness of the PSEHTT:$IC_{60}BA$ film, resulting in the increase in the electric resistance of PSEHTT:$IC_{60}BA$, because the increase in the resistance induced the increase in the probability of charge recombination in the PSEHTT:$IC_{60}BA$. The external quantum efficiency (EQE) spectra for these single junction PSCs (Fig. 2b) are consistent with the J_{sc} obtained from the *J–V* characteristics (Fig. 2a). The integrated J_{sc} values can be obtained from the ESI (Table S1†). The EQE increases at around 350 nm and 625 nm, as the thickness of the PSEHTT:$IC_{60}BA$ increases from 70 nm to 80 nm. Nevertheless, no change in the EQE above 625 nm was recognized when the thickness of PSEHTT:$IC_{60}BA$ was varied. As we further increased the thickness of PSEHTT:$IC_{60}BA$ to 100 nm, the device performance worsened due to the reduced light absorption. Note that the film morphology can be changed (greatly influenced) by the spin coating speed.

In the next optimization experiment, the thickness of the PTB7:$PC_{71}BM$ was changed, while the thickness of the PSEHTT:$IC_{60}BA$ front subcell was fixed at 80 nm (900 rpm), with MoO_3 as the hole transport layer. The results of their photovoltaic performance and *J–V* curves are shown in Table 2 and Fig. 3a, respectively, with different thicknesses from 90 nm to 120 nm under the illumination of AM 1.5G, 100 mW cm^{-2}. For all devices, the V_{oc} was independent of the spin coating speed. The J_{sc} and PCE increased with a thickness of up to 100 nm. The J_{sc} of the single-junction PSCs was enhanced from 14.86 ± 0.01 to 15.24 ± 0.03 mA cm^{-2} as the thickness of PTB7:$PC_{71}BM$ increased to 120 from 90 nm. The highest J_{sc} of 15.54 ± 0.02 mA cm^{-2} (M = 1.04 ± 0.02) was obtained from 100 nm and the value was 1.97% higher than that of 120 nm.

Despite the higher absorption in the thicker films, the J_{sc} was reduced from 15.54 ± 0.02 mA cm^{-2} to 15.24 ± 0.03 mA cm^{-2} with an increased PTB7:$PC_{71}BM$ thickness of 100 nm to 120 nm. The FF remained relatively constant as the thickness of the PTB7:$PC_{71}BM$ increased up to 120 nm. This indicates that the morphology and recombination do not severely limit the device performance as the thickness of PTB7:$PC_{71}BM$ increases. Overall, the optimal thickness of PTB7:$PC_{71}BM$ was found to be 100 nm with a high PCE of 8.08%. In contrast, the control device (fabricated with PEDOT:PSS) showed a PCE of 7.25 ± 0.01%. The maximum EQE is almost 80%, which indicates an efficient photon-to-electron conversion. Fig. 3b demonstrates that the device EQE depends on the photosensitive material thickness. The integrated EQE values are in good agreement with the J_{sc} values obtained from Fig. 3a. The integrated J_{sc} values can be obtained from the ESI (Table S2†).

The inverted tandem solar cell architecture consists of a wide bandgap polymer front subcell, the ICL, along with a medium

Table 2 Device performance of PTB7:$PC_{71}BM$-based single junction solar cells with different photosensitive thicknesses and different HTLs. The values in Table 2 are the average of 63 devices

PTB7:$PC_{71}BM$ thickness (nm)	HTL	J_{sc} (mA cm^{-2})	V_{oc} (V)	FF (%)	PCE (%)	M
90	MoO_3	14.86 ± 0.01	0.76 ± 0.01	65.49 ± 0.02	7.39 ± 0.02	1.02 ± 0.01
100	MoO_3	15.54 ± 0.02	0.76 ± 0.01	68.24 ± 0.01	8.08 ± 0.01	1.04 ± 0.02
110	MoO_3	15.42 ± 0.02	0.76 ± 0.01	68.31 ± 0.01	8.01 ± 0.02	0.94 ± 0.02
120	MoO_3	15.24 ± 0.03	0.76 ± 0.01	68.83 ± 0.02	7.98 ± 0.01	0.99 ± 0.01
80	WO_3	13.70 ± 0.01	0.75 ± 0.01	63.80 ± 0.01	6.52 ± 0.02	1.08 ± 0.01
70	PEDOT:PSS	14.80 ± 0.11	0.74 ± 0.01	66.40 ± 0.02	7.25 ± 0.01	1.03 ± 0.03

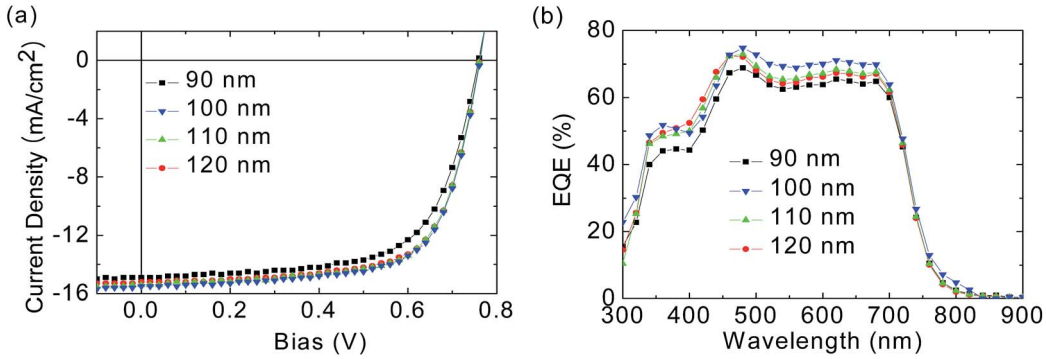

Fig. 3 PTB7:$PC_{71}BM$-based single junction solar cells performance with different photosensitive thicknesses and MoO_3 HTL under AM 1.5G illumination (25 °C, 100 mW cm^{-2}). (a) *J–V* curves. (b) External quantum efficiency.

bandgap polymer bottom subcell. It is a useful way to harvest a broader part of the solar spectrum and more efficient use of photon energy than the single junction solar cell. A polymer tandem solar cell with an inverted configuration was fabricated using: a front subcells donor polymer, a bottom subcell donor polymer, a front subcell acceptor material, and a bottom acceptor material of PSEHTT, PTB7, $IC_{60}BA$, and $PC_{71}BM$, respectively. Fig. 4a demonstrates the simulation contour plot as a function of different thicknesses for the front and bottom subcells. One could achieve a maximum efficiency of 12% with suitable front and bottom subcell thicknesses (Fig. 4a). The inverted tandem PSC is ITO/LZO (40 nm)/C_{60}-SAM (10 nm)/PSEHTT:$IC_{60}BA$ (80 nm)/pH-neutral PEDOT:PSS (20 nm)/LZO (30 nm)/$C_{60\text{-SAM}}$ (10 nm)/PTB7:$PC_{71}BM$ (100 nm)/MoO_3 (30 nm)/Ag (100 nm) (shown in Fig. 1c). Fig. 1d shows the energy level diagram of the fabricated inverted tandem PSC.

Fig. 4b shows the illuminated *J–V* curves of the inverted single junction front subcell, the bottom subcell, and tandem PSCs. The front subcell with a 80 nm PSEHTT:$IC_{60}BA$ layer yields a PCE of 6.59 ± 0.01%, a V_{oc} of 0.94 ± 0.01 V, a J_{sc} of 10.65 ± 0.02 mA cm^{-2}, and a FF of 65.84 ± 0.03%. The bottom subcell with a 100 nm PTB7:$PC_{71}BM$ layer exhibits a PCE of 8.08

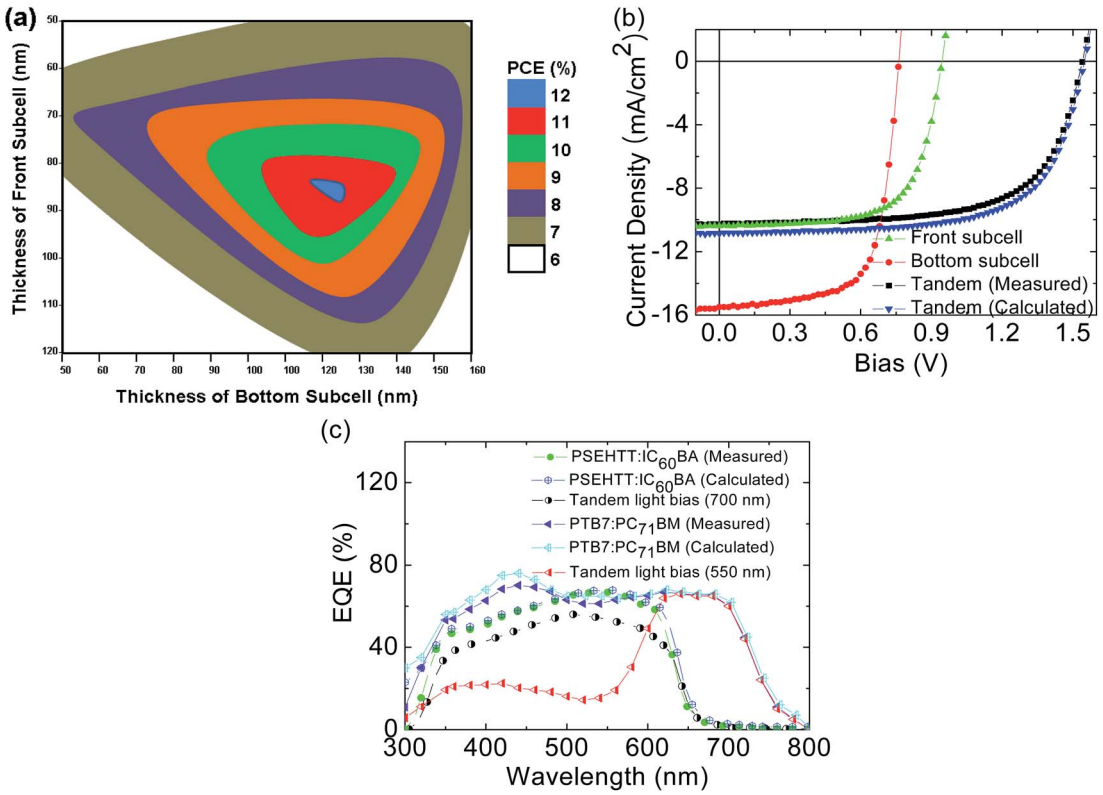

Fig. 4 (a) Simulation efficiency generated in an inverted double-junction tandem PSC as a function of the front and bottom thicknesses. (b) *J–V* curves of front, bottom, and inverted tandem PSCs under AM 1.5G illumination (25 °C, 100 mW cm^{-2}). (c) EQE measured under relevant bias illumination conditions.

± 0.01%, a V_{oc} of 0.76 ± 0.01 V, a J_{sc} of 15.54 ± 0.02 mA cm^{-2}, and a FF of 68.24 ± 0.01%. The average PCE of 34 tandem cells is 10.39 ± 0.03% with a V_{oc} of 1.54 ± 0.01 V, a J_{sc} of 10.30 ± 0.01 mA cm^{-2} (M = 0.97 ± 0.03), and a FF of 65.47 ± 0.02% (Table 3). In general, the ideal V_{oc} for tandem devices is the exact summation of the front and bottom subcells. The V_{oc} of our tandem device is 1.54 V, indicating a slight loss compared to the high performing ICL. The FF (65.47%) of the tandem device is slightly lower than the average value of the front and bottom subcells (65.74% for the front subcell and 68.24% for the bottom subcell). Fig. 4c demonstrates the EQE spectra of the front, bottom, and tandem cells from a 300 nm to 800 nm wavelength. One should note that the EQE measurements of the tandem solar cell require specific precaution in regard to coupled light absorption and current-generation processes in each subcell.[47] EQE measurements were carried out with two excitation light sources; 700 nm and 550 nm light optical bias light beams. The EQE spectra reveal a desirable match in the photocurrents generated by both subcells. The EQE spectra closely follow the absorption spectra of the front and bottom subcells, corresponding to the photocurrents rendered from photosensitive layers.[43,45] The integrated J_{sc} values can be obtained from the ESI (Table S3†).

Before we proceeded with the fabrication of inverted triple-junction PSCs, we carried out the optimization of a single junction PSC based on poly[2,5-bis(2-hexyldecyl)-2,3,5,6-tetrahydro-3,6-dioxopyrrolo[3,4*c*]pyrrole-1,4-diyl]-*alt*-[3′,3″-dimethyl-2,2′:5′,2″-terthiophene]-5,5″-diyl (PMDPP3T, E_{g3} = 1.3 eV) blended with $PC_{70}BM$.[39] The performance of PSCs with PMDPP3T:$PC_{70}BM$ was further optimized by changing the thickness with different spin coating speeds and was characterized under simulated AM 1.5G illumination at 100 mW cm^{-2} (Fig. 5 and Table 4).

As can be seen in Fig. 5a, the photovoltaic performance of the PMDPP3T:$PC_{70}BM$-based PSCs depends strongly on the thickness of the photosensitive layer. The increased J_{sc} of the PMDPP3T:$PC_{70}BM$ from 17.10 ± 0.01 mA cm^{-2} to 17.51 ± 0.01 mA cm^{-2} (M = 0.95 ± 0.01) is attributed primarily to a redistribution of light intensity in the photosensitive layer. All of the devices with different thicknesses of PMDPP3T:$PC_{70}BM$ film resulted in a comparable V_{oc} of ~0.60 V, which is reasonable because V_{oc} is governed by the energetic relationship between the donor and acceptor in the BHJ-based PSCs.[48,49] The FF of our devices shows a considerable increase from 110 nm (55.98 ± 0.02%) to 120 nm (60.29 ± 0.01%), which is due to the reduction of series resistance. In addition, with the increase of the PMDPP3T:$PC_{70}BM$ thickness from 120 nm to 130 nm, the J_{sc} obviously decreased from 17.51 ± 0.01 mA cm^{-2} to 16.68 ± 0.03 mA cm^{-2}, directly resulting from a great decrease in PCE from 6.33 ± 0.01% to 6.11 ± 0.01%, as shown in Table 4. It is worth noting that J_{sc} and PCE do not increase further, even if the PMDPP3T:$PC_{70}BM$ thickness is continuously increased (from 130 nm to 140 nm). Therefore, there is an optimal PMDPP3T:$PC_{70}BM$ thickness to the PSC performance. The overall PCE in the device with 120 nm reaches 6.33 ± 0.01%. This is slightly lower than previously reported work by Jannsen.[39]

The EQE spectra for PMDPP3T:$PC_{70}BM$-based PSCs are shown in Fig. 5b. As we can see from these spectra, the inverted single-junction PSCs with 120 nm demonstrated the maximum EQE of 58%, which corresponds to efficient photo-to-electron conversion. However, the lowest EQE comes from the cells with a 140 nm of PMDPP3T:$PC_{70}BM$, where the maximum EQE is 45%. Moreover, for all PMDPP3T:$PC_{70}BM$-based devices, the integral current density deduced by the EQE spectra are in good agreement with our experimentally recorded J_{sc} values. The integrated J_{sc} values can be obtained from the ESI (Table S4†). The difference between the measured J_{sc} and the calculated current density value are within 5%, indicating that the photovoltaic measurement is reliable.

Despite the growing interest in developing high performance donor materials, one alternative, but complicated approach to enhance the efficiency of the polymer tandem solar cell and to achieve an even higher V_{oc} (series connected) is through stacking up an additional low bandgap third subcell. In this study, we used the inverted triple-junction PSC *via* a 1 + 1 + 1 configuration to achieve a higher photoresponse. In order to harvest most of the light in the window down to 960 nm, the ideal candidate for this complementary absorption should possess a 1.3 eV low bandgap. This is one of the reasons why we selected PMDPP3T:$PC_{70}BM$ to serve as our bottom subcell. Additionally, we also carried out electrical optical simulations on various triple-junction configuration thicknesses to balance the rates of photon absorption among the subcells and to maximize the current-balancing conditions, using the characteristics of the individual photosensitive layers. Thus, we propose that such 1 + 1 + 1 triple-junction cells can provide increased efficiency, as well as a higher V_{oc} compared to that of double-junction tandem cells.

We selected copolymer PMDPP3T blended with $PC_{70}BM$ (Fig. 6a) to serve as the bottom subcell. The extinction coefficient of PMDPP3T:$PC_{70}BM$ is shown in Fig. 6b. Fig. 6c and d

Table 3 Device performances of front, bottom, and tandem cells under AM 1.5G illumination (25 °C, 100 mW cm^{-2})

Structure	J_{sc} (mA cm^{-2})	V_{oc} (V)	FF (%)	PCE (%)	M
Front subcell	10.65 ± 0.02	0.94 ± 0.01	65.84 ± 0.03	6.59 ± 0.01	1.08 ± 0.02
Bottom subcell	15.54 ± 0.02	0.76 ± 0.01	68.24 ± 0.01	8.08 ± 0.01	1.04 ± 0.02
Tandem cell (M)[a]	10.30 ± 0.01	1.54 ± 0.01	65.47 ± 0.02	10.39 ± 0.03	0.97 ± 0.03
Tandem cell (C)[b]	10.88	1.54	66.26	11.10	—

[a] M = measured. [b] C = calculated.

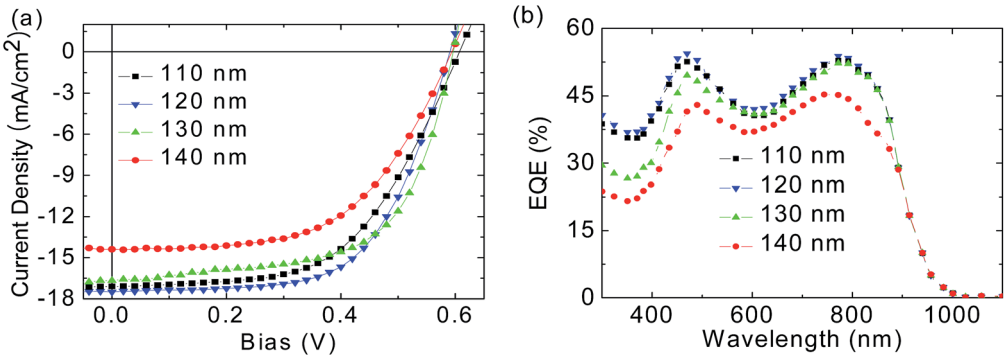

Fig. 5 PMDPP3T:$PC_{70}BM$-based single junction solar cells performance with different photosensitive thicknesses and LZO ETL under 1 sun, AM 1.5G illumination (25 °C, 100 mW cm^{-2}). (a) *J–V* curves. (b) External quantum efficiency.

show the complete triple-junction PSC device structure, and their respective energy levels. The first ICL consists of 100 nm pH-neutral PEDOT:PSS, 100 nm LZO, and 10 nm C_{60}-SAM; and the second ICL comprises 50 nm pH-neutral PEDOT:PSS, 50 nm LZO, and 10 nm C_{60}-SAM, which are used between the front and middle subcell, and the middle and bottom subcells, respectively to ensure minimal absorption loss. Compared to that of the tandem cell (presented before), the thicknesses of all the subcells increased according to the simulated efficiency, as shown in Fig. 6e. This increase is due to the fact that the front and middle absorbing subcells absorb at different optical maxima to efficiently harvest short wavelength photons, while at the same time complementing the absorption of the bottom NIR absorbing subcell. Using this approach, the triple-junction solar cell exhibited a PCE of 11.83 ± 0.02%, exceeding the previous record set by Yang *et al.*,[41] along with a V_{oc} of 2.24 V ± 0.01 V, a FF of 67.52 ± 0.03%, and a J_{sc} of 7.83 ± 0.03 mA cm^{-2} ($M = 1.01 \pm 0.02$), suggesting a huge potential for future multi-junction PSCs research.

The *J–V* characteristics of the single (front, middle, and bottom subcells), inverted tandem, and inverted triple-junction PSCs are compared in Fig. 6f, with the performance parameters tabulated in Table 5. Compared to the tandem cell, the V_{oc} of the triple-junction PSC increased to 2.24 ± 0.01 V from 1.54 ± 0.01 V. One should note that the increase in V_{oc} resulted in increases in PCE from 10.39 ± 0.03% to 11.83 ± 0.02% being recorded.

Note also that the V_{oc} is 0.06 V lower than the sum of its subcells, mainly due to the reduced optical intensity in each photosensitive layer. We also investigated the decrease in photocurrent (from 10.30 ± 0.01 mA cm^{-2} to 7.83 ± 0.03 mA cm^{-2}) using EQE measurements (Fig. 6g). Furthermore, the integrated current density was deduced by the EQE spectra, and is in good agreement with the values of the experimental J_{sc}. The integrated J_{sc} values can be obtained from the ESI (Table S5†). The EQE spectra of the front, middle, and bottom subcells closely resemble those of the double junction cell.

Today, we have seen rapid improvement in PCE; however, another important issue in PSCs lies in their lifetime. Degradation mechanisms typically involve morphological changes,[50] deterioration of material (active layer, electrode, and interfacial layer) by oxygen and water, interlayer and electrode diffusion, and electrode reaction with the organic materials.[51] McGehee *et al.* demonstrated an extremely long lifetime of the regular device of up to seven years by employing poly[9′-hepta-decanyl-2,7-carbazole-*alt*-5,5-(4′,7′-di-2-thienyl-2′,1′,3′ benzothiadiazole) (PCDTBT):[6,6]-phenyl-C_{71} butyric acid methyl ester ($PC_{71}BM$) by limiting the oxygen and water.[52] Meanwhile, Frechet *et al.* suggested that materials engineered with cross-linkable materials are able to block morphology development and stabilize a regular device.[53,54] Heeger *et al.* also established that interfacial engineering can possibly improve device stability by the introduction of titanium oxide (TiO_x) as a cathode interfacial layer and by replacing our frequently used PEDOT:PSS with MoO_x.[55] The PCE of their regular devices declined to approximately 50% of the initial value after 720 h storage in ambient air. This is a great improvement compared to their control device, where the

Table 4 Device performance of PMDPP3T:$PC_{70}BM$-based single junction solar cells with different photosensitive thicknesses and different ETLs. The values in Table 4 are the average of 56 devices

PMDPP3T:$PC_{70}BM$ thickness (nm)	ETL	J_{sc} (mA cm^{-2})	V_{oc} (V)	FF (%)	PCE (%)	*M*
110	LZO	17.10 ± 0.01	0.60 ± 0.01	55.98 ± 0.02	5.74 ± 0.02	0.97 ± 0.03
120	LZO	17.51 ± 0.01	0.60 ± 0.01	60.29 ± 0.01	6.33 ± 0.01	0.95 ± 0.01
130	LZO	16.68 ± 0.03	0.60 ± 0.01	61.03 ± 0.04	6.11 ± 0.01	1.04 ± 0.02
140	LZO	14.40 ± 0.02	0.60 ± 0.01	55.21 ± 0.02	4.77 ± 0.03	1.02 ± 0.03
120	TiO_x	16.33 ± 0.02	0.60 ± 0.01	57.11 ± 0.02	5.60 ± 0.01	1.06 ± 0.01
130	GO	16.93 ± 0.02	0.60 ± 0.01	44.40 ± 0.03	4.51 ± 0.02	0.99 ± 0.02

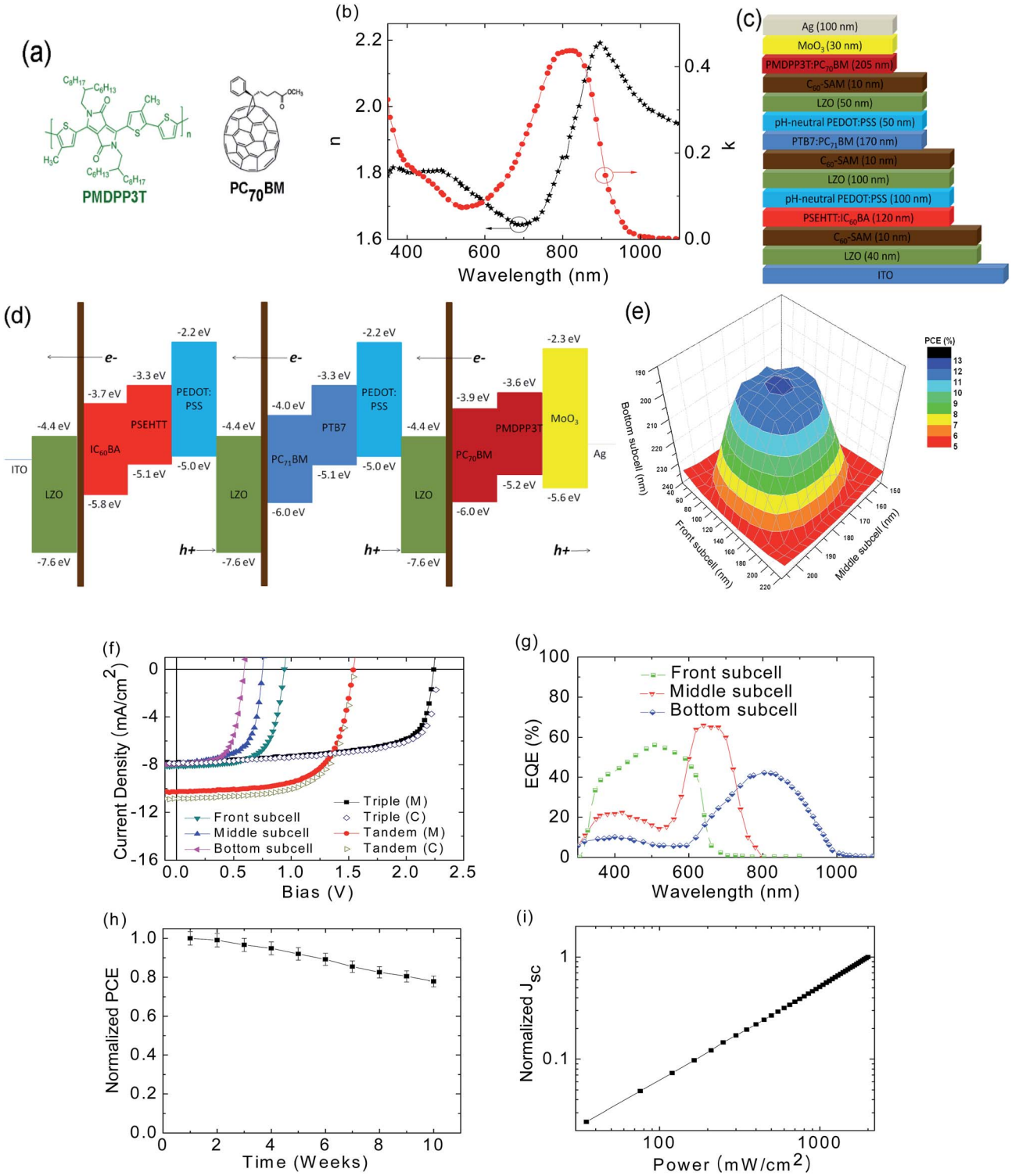

Fig. 6 (a) Molecular structures of the near infrared absorbing copolymer PMDPP3T, and $PC_{70}BM$ fullerenes. (b) Optical parameters *n* and *k* for PMDPP3T:$PC_{70}BM$. (c) Inverted triple-junction PSCs:ITO/LZO/C_{60}-SAM/PSEHTT:$IC_{60}BA$/pH-neutral PEDOT:PSS/LZO/C_{60}-SAM/PTB7:$PC_{71}BM$/pH-neutral/LZO/C_{60}-SAM/PMDPP3T:$PC_{70}BM$/MoO_3/Ag. (d) Energy band diagram of inverted triple-junction PSCs. Predicted (e) efficiency of inverted triple-junction PSCs as functions of the thicknesses of the PSEHTT:$IC_{60}BA$ front subcell, the PTB7:$PC_{71}BM$ middle subcell, and the PMDPP3T:$PC_{70}BM$ bottom subcell. (f) *J*–*V* curves of front, middle, bottom, tandem and triple-junction cells under AM 1.5G illumination (25 °C, 100 mW cm^{-2}). (g) EQE measured under relevant bias illumination conditions. (h) Stability of the inverted triple-junction PSCs over 10 weeks. (i) Normalized (to the value obtained at 2000 mW cm^{-2}) J_{sc} of inverted triple-junction solar cells as a function of illumination intensity. Inverted triple-junction PSCs show a linear dependence on the illumination intensity up to 2000 mW cm^{-2}.

Table 5 Device performance of front, middle, bottom, tandem and inverted triple-junction PSCs under AM 1.5G illumination (25 °C, 100 mW cm^{-2})

Configuration	J_{sc} (mA cm^{-2})	V_{oc} (V)	FF (%)	PCE (%)	M
Front subcell	8.10 ± 0.02	0.94 ± 0.01	66.39 ± 0.02	5.06 ± 0.03	1.08 ± 0.02
Middle subcell	8.00 ± 0.02	0.76 ± 0.01	67.03 ± 0.03	4.08 ± 0.04	1.04 ± 0.02
Bottom subcell	7.94 ± 0.03	0.60 ± 0.01	63.17 ± 0.01	3.01 ± 0.02	1.02 ± 0.01
Tandem (M[a])	10.30 ± 0.01	1.54 ± 0.01	65.47 ± 0.02	10.39 ± 0.03	0.97 ± 0.03
Tandem (C[b])	10.88	1.54	66.26	11.10	—
Triple (M[a])	7.83 ± 0.03	2.24 ± 0.01	67.52 ± 0.03	11.83 ± 0.02	1.01 ± 0.02
Triple (C[b])	7.93	2.30	67.39	12.18	—

[a] M = measured. [b] C = calculated.

efficiency decreased approximately 90% from its initial value after just 480 h.

It has been generally accepted that the inverted architecture usually demonstrates better stability,[56–60] hence our encapsulated device also shows a good lifetime in ambient air over 10 weeks. Fig. 6h shows the shelf life test in air, where an initial efficiency of 11.83% survived the five weeks degradation test; whereby, the efficiency only dropped by 8.73%. However, after 10 weeks the efficiency plunged by 28.45%. Although, we understood that the inverted structure always provides a better lifetime, our device still suffered some degradation. Nonetheless, these observations demonstrate that, although encapsulation can be considered to be one alternative to alleviate the degradation process, detailed and comprehensive work is still needed to fully understand the real degradation mechanism and to further enhance the shelf life of one particular cell.

In addition, the normalized J_{sc} of the inverted triple-junction PSCs with optimized ICL demonstrated a linear dependence on the illumination intensity, as shown in Fig. 6i. The J_{sc} was normalized to that obtained under 2000 mW cm^{-2}. Even though executed at higher light intensities (~2000 mW cm^{-2}), there is no clear indication to support that a substantial space charge build up in the device would cause enhanced carrier recombination and a sublinear dependence of J_{sc} on the illumination intensity.

Moreover, optimization of the BHJ layers' thicknesses is crucial for obtaining high performance inverted triple-junction PSCs. To access in detail, the balanced optical absorption and current matching, the front, middle, and bottom subcells' BHJ layer thicknesses must be optimized. As it is seen, our inverted triple-junction PSCs are limited by the photocurrent of the front subcell, thus we performed another optimization to determine what the best current balancing conditions are. The J_{sc} generated by each subcell must be similar in order to avoid any build-up of photogenerated charge, which would bias the affected cells away from the optimal point, resulting in a lower efficiency. Thus, the J_{sc} can be balanced by varying the thickness of each subcell in the stack. Regardless, in inverted triple-junction PSCs with identical or different BHJ layers, the number of absorbed photons from the incident solar energy[61] and the charge carrier transport, as well as the bimolecular recombination of charge carriers,[62] must be optimized to match the photocurrents between all the subcells. Low charge carrier mobilities and unbalanced electron/hole mobilities in the PSCs[63,64] are characteristics of PSCs that make it challenging to balance current densities between those subcells. Hence, a series of inverted triple-junction PSCs were carefully designed to examine the influence of all the subcell thicknesses on the performance of the devices.

One can see that the simulated J_{sc} for inverted triple-junction PSCs is able to reach the maxima of 9 mA cm^{-2} (Fig. 7a). We varied the thickness of those subcells accordingly to balance the current, as well as to maintain an adequate absorption and photocurrent in the bottom subcell.

Fig. 7b illustrates the J–V curves of various sets of inverted triple-junction PSCs with different BHJ thicknesses. The extracted photovoltaic parameters obtained from the J–V curves are summarized in Table 6. In the current balancing purpose experiment, we observed that the prepared inverted triple-junction PSCs exhibited an identical V_{oc} of ~2.24 V, which is slightly less than that of the ideal summation value of the V_{oc} values for all the subcells. As shown in Table 6, the performance changes with various photosensitive material thicknesses.

As the PMDPP3T:PC_{70}BM BHJ thickness decreases from 205 nm to 195 nm, the inverted triple-junction PSCs still perform well. The FF varies with the changes of the bottom subcells. Despite some variations in FF, one also sees a decrease in J_{sc} from 7.83 ± 0.03 mA cm^{-2} to 6.97 ± 0.02 mA cm^{-2}, which yields a considerable decrease in PCE, with PCE dropping from 11.83 ± 0.02% to 10.51 ± 0.01%. Similarly, as the thickness of PSEHTT:IC_{60}BA increases to 130 nm and the PTB7:PC_{71}BM decreases to 165 nm, the inverted triple-junction PSCs decreased in both the J_{sc} and FF. This leads to a reduction in efficiency down to 11.09 ± 0.03% from 11.83 ± 0.02%. In the case of the 115 nm thickness of the PSEHTT:IC_{60}BA front subcell, the J_{sc} is almost the same as with the average inverted triple-junction PSCs of about 7.73 ± 0.01 mA cm^{-2}. Conversely, the PCE greatly decreases to 10.54 ± 0.01%, due to the significant reduction of FF from 67.52 ± 0.03% to 60.90 ± 0.03%. From this data, one can conclude that the thicknesses of all the subcells are strongly influenced by the performance of the device. Therefore, a careful design, along with suitable bandgap

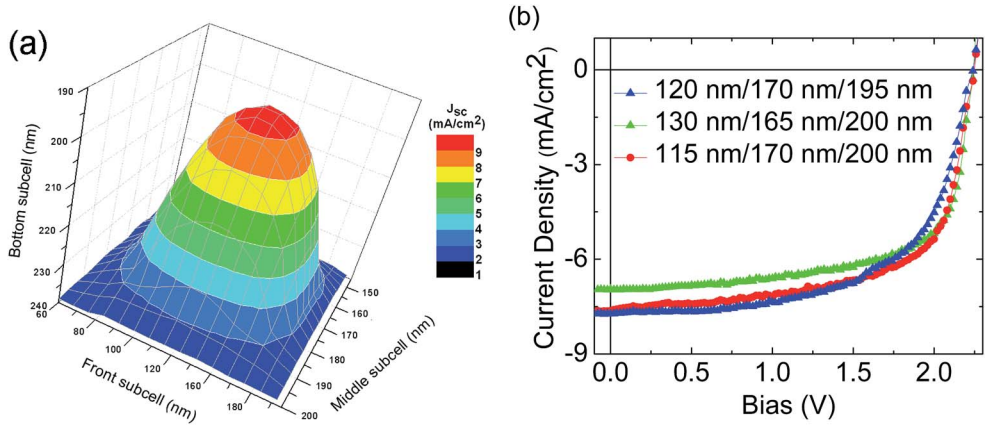

Fig. 7 (a) Predicted short-circuit current density for inverted triple-junction PSCs as a function of the thicknesses of the PSEHTT:$IC_{60}BA$ front subcell, PTB7:$PC_{71}BM$ middle subcell, and the PMDPP3T:$PC_{70}BM$ bottom subcell under 1 sun, AM 1.5G illumination (25 °C, 100 mW cm^{-2}). (b) *J–V* curves of inverted triple-junction PSCs with various thicknesses of front, middle, and bottom subcells.

engineering, is important when developing a high performance device.

In order to check the reproducibility of our results, 69 inverted triple-junction PSCs were fabricated and measured using optimized front, middle, and bottom subcell thicknesses.

Histograms of the photovoltaic parameters are demonstrated in Fig. 8. As shown in Fig. 8, these inverted triple-junction PSCs are highly reproducible.

In a multi-junction solar cell, ICL has many functions, such as to optically and electrically connect all the subcells in the multiple stacks and to protect the underneath subcell from any solvent penetration during the deposition of the subsequent subcell. To understand the effect of the different ICLs on the device performance, we fabricated inverted triple-junction PSCs with a structure of ITO/LZO/C_{60}-SAM/PSEHTT:$IC_{60}BA$/ICL/C_{60}SAM/PTB7:$PC_{71}BM$/ICL/C_{60}-SAM/PMDPP3T:$PC_{70}BM$/MoO_3/Ag.

Fig. 9 and Table 7 summarize the *J–V* characteristics and the photovoltaic parameters of the inverted triple-junction PSCs with four different ICLs under 100 mW cm^{-2} AM1 5G illumination, respectively.

It is worth noting that the ICL should efficiently collect electrons from one cell and holes from another, and function as an efficient recombination region for them, free of potential loss.[65,66] Based on the characterization of the front, middle, and bottom single-junction PSCs, inverted triple-junction PSCs with MoO_3/Al/LiF, MoO_3/Ag/LiF, MoO_3/Au/LiF, and no ICLs were prepared and characterized. It was demonstrated that the ICL completely influences the performance of the devices. As expected, the device without the presence of ICL showed a poorer performance with a J_{sc} of 5.83 ± 0.02 mA cm^{-2}, a V_{oc} of 1.22 ± 0.01 V, a FF of 51.92 ± 0.02%, and a PCE of 3.69 ± 0.13%. The poor performance indicated that the front, middle, and bottom subcells were not electrically connected in series. Moreover, it was demonstrated that the device with MoO_3/Au/

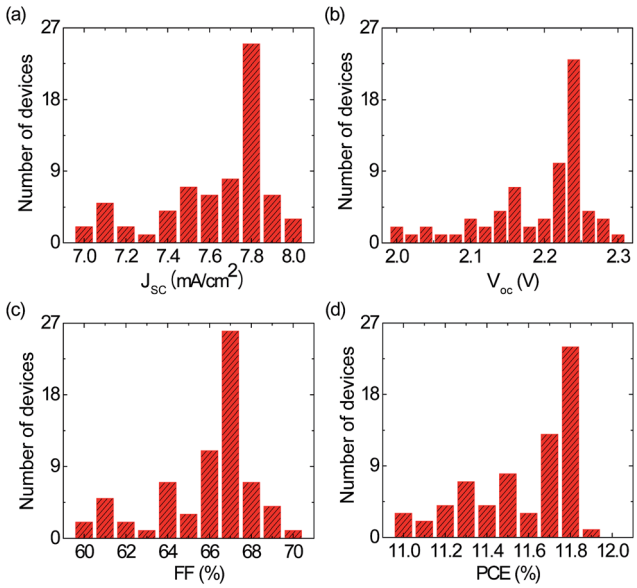

Fig. 8 Histogram of inverted triple-junction PSCs parameters measured for 69 separate devices under 1 sun, AM 1.5G illumination (25 °C, 100 mW cm^{-2}). J_{sc} (a), V_{oc} (b), FF (c), and PCE (d).

Table 6 Device performance of inverted triple-junction PSCs with different front, middle, and bottom subcell thicknesses

Photosensitive thickness (front/middle/bottom) [nm]	J_{sc} (mA cm^{-2})	V_{oc} (V)	FF (%)	PCE (%)	*M*
120/170/195	6.97 ± 0.02	2.24 ± 0.01	67.60 ± 0.02	10.51 ± 0.01	1.01 ± 0.02
130/165/200	7.63 ± 0.01	2.24 ± 0.01	64.90 ± 0.02	11.09 ± 0.03	0.97 ± 0.03
115/170/200	7.73 ± 0.01	2.24 ± 0.01	60.90 ± 0.03	10.54 ± 0.01	0.99 ± 0.02

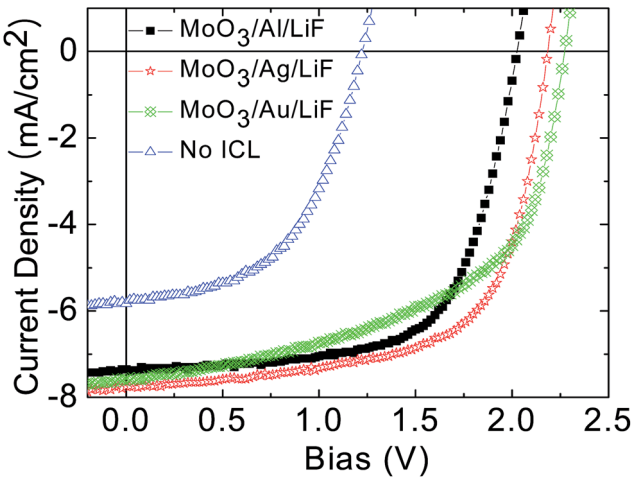

Fig. 9 J–V curves of inverted triple-junction PSCs with different ICLs under 1 sun, AM 1.5G illumination (25 °C, 100 mW cm^{-2}).

Table 7 Device performance of inverted triple-junction PSCs with different interconnecting layers

ICL	J_{sc} (mA cm^{-2})	V_{oc} (V)	FF (%)	PCE (%)
MoO_3/Ag/LiF	7.35 ± 0.04	2.02 ± 0.02	65.98 ± 0.01	9.80 ± 0.04
MoO_3/Au/LiF	7.75 ± 0.03	2.18 ± 0.01	65.16 ± 0.11	11.01 ± 0.01
MoO_3/Al/LiF	7.58 ± 0.02	2.28 ± 0.01	54.77 ± 0.03	9.46 ± 0.02
No ICL	5.83 ± 0.02	1.22 ± 0.01	51.92 ± 0.02	3.69 ± 0.13

LiF ICL showed a J_{sc} of 7.75 ± 0.03 mA cm^{-2}, a V_{oc} of 2.18 ± 0.01 V, and a FF of 65.16 ± 0.11%, along with a PCE of 11.01 ± 0.01%. The V_{oc} of 2.18 V of the device is 94% of the ideal summation of the V_{oc} (2.3 V). Overall, the inverted triple-junction PSCs are electrically connected by the MoO_3/Au/LiF ICL. For the inverted triple-junction PSCs with a MoO_3/Al/LiF ICL, the results showed a J_{sc} of 7.58 ± 0.02 mA cm^{-2}, a V_{oc} of 2.28 ± 0.01 V, a FF of 54.77 ± 0.03%, and a PCE of 9.46 ± 0.02%. While in the case of MoO_3/Ag/LiF, the device delivered a J_{sc} of 7.35 ± 0.04 mA cm^{-2}, a V_{oc} of 2.02 ± 0.02 V, a FF of 65.98 ± 0.01%, and a PCE of 9.80 ± 0.04%. In comparison with MoO_3/Al/LiF ICL, the higher FF values (for MoO_3/Ag/LiF and MoO_3/Au/LiF) are attributed to the fact that the low work functions of Ag (4.26 eV), Au (5.1 eV), and LiF (2.6 eV) are an energy step for efficient charge recombination zones for the hole extracted from the front and middle subcells through MoO_3 and for the electrons extracted from the middle and bottom subcells through LiF. Moreover, it was demonstrated that although the V_{oc} of the inverted triple-junction PSCs of the MoO_3/Al/LiF device is slightly higher than that of other devices, the FF is much smaller compared to the rest of the devices. This may not only be attributed to the formation of an oxide layer between MoO_3 and LiF, but also to a bad redistribution of the built-in electric field in the subcells employed with MoO_3/Al/LiF. In addition, the Pauling electro-negativity values of Ag and Au (1.93 eV and 2.54 eV, respectively) are closer to that of Mo than that of Al, and thus avoid oxide formation, which would decrease the series resistance in devices.

Conclusions

In summary, we demonstrated solution-deposited inverted tandem PSCs and inverted triple-junction PSCs. The tandem PSCs employ wide and medium bandgap polymers with minimal overlap in their absorption spectra. The optimized inverted tandem PSCs demonstrate a PCE of 10.39 ± 0.03% with J_{sc} = 10.30 ± 0.01 mA cm^{-2}, V_{oc} = 1.54 ± 0.01 V, and FF = 65.47 ± 0.02% under AM 1.5G 1 sun intensity (spectrally corrected).

Moreover, we fabricated the inverted triple-junction PSCs by adding an additional low bandgap copolymer PMDPP3T blended $PC_{70}BM$ as the bottom subcell that absorbs photons up to 960 nm. The improved current balancing is due to a careful bandgap engineering of $E_{g1} > E_{g2} > E_{g3}$. With such bandgap engineering, our inverted triple-junction PSCs reached a PCE of 11.83 ± 0.01%, exceeding the record efficiency of tandem PSCs and triple-junction solar cell, previously reported by others along with a J_{sc} = 7.83 ± 0.03 mA cm^{-2}, V_{oc} = 2.24 ± 0.01 V, and FF = 67.52 ± 0.03% under AM 1.5G 1 sun intensity (spectrally corrected). The optical simulation allows us to surpass the complexity of current balancing issues between the subcells, and thus to subsequently simplify the optimization process of the thickness for all the subcells. The agreement between the experimental data and the simulated results clearly demonstrate the feasibility and accuracy of using optical modelling in the design of multi-junction polymer solar cells; especially in optimizing the thicknesses of the subcell. Solution-processed and low-temperature multi-junction solar cells basically allow us to fabricate polymer solar cells with an unlimited number of subcells. Thus, the triple-junction polymer solar cell still has considerable room for improvement, both in terms of photogenerated current density, open circuit voltage, as well as efficiency.

Experimental

Materials

The polymers PSEHTT and PMDPP3T were synthesized according to the previously reported methods.[43,39] The polymer PTB7 was received from 1-materials. All fullerenes $IC_{60}BA$, $PC_{71}BM$, and $PC_{70}BM$, as well as pH-neutral PEDOT:PSS were purchased from Sigma Aldrich. All the materials used in this study were purified once using temperature-gradient sublimation.[2]

Single junction fabrication (front subcell)

The pre-cleaned ITO substrates were first treated with UV-ozone for 10 min. The literature reported procedure was followed to prepare the LZO film.[19] Afterward, the solution was spin-coated onto the ITO substrate at a spin speed of 700 rpm for 1 min (and baked at 100 °C for 3 min). The approximate thickness of the film is 40 nm. Subsequently, a C_{60}-SAM layer was deposited onto the LZO using the spin-coating process, as previously reported.[67] The substrate was washed with THF twice to remove unbound C_{60}-SAM molecules. Then, the photosensitive layer was spin-coated onto the LZO/C_{60}-SAM layer. PSEHTT:$IC_{60}BA$ (1 : 1, weight ratio) was dissolved in a solvent mixture of

1,2-dichlorobenzene (ODCB) and 1,8-octanedithiol (ODT) (ODCB:ODT = 100 : 2.5, v/v) for the front photosensitivity at 800 rpm for 1 min and annealed at 100 °C for 3 min. Next, 20 nm pH-neutral PEDOT:PSS was spin-coated at 900 rpm for 1 min and baked for 120 °C for 1 min. After spin-coating the photosensitive layer, the samples were transferred into the evaporation chamber for thermal evaporation of the 30 nm MoO_3 and 100 nm Ag electrode. The device area was 0.1 cm^2.

Single junction fabrication (middle subcell)

The pre-cleaned ITO substrates were first treated with UV-ozone for 10 min. ETL (LZO/C_{60}-SAM) was spin-coated on the ITO substrates. Then, the photosensitive layer was spin-coated onto the ETL layer. The middle subcell photosensitive layer was spin-coated at 1500 rpm for 1 min from the PTB7:PC_{71}BM (1 : 1.5) and dissolved in 97% chlorobenzene with 3% 1,8-diiodooctane, DIO, at a concentration of 10 mg mL^{-1}. Then, it was left idle for 1 h to remove residual DIO in a glovebox, followed by the deposition of 20 nm pH-neutral PEDOT:PSS at a spin speed of 900 rpm and annealed at 120 °C for 1 min. Finally, the samples were transferred into the evaporation chamber to evaporate the 30 nm MoO_3 and 100 nm Ag electrode. The device area was 0.1 cm^2.

Single junction fabrication (bottom subcell)

Single-junction photovoltaic devices based on low bandgap copolymers were started by spin-coating the bilayer ETL (LZO/C_{60}-SAM) onto pre-cleaned, patterned ITO substrates in air (14 Ω per square). Later, the PMDPP3T:PC_{70}BM photosensitive layer was solution deposited by spin-coating from a mixture of chloroform and *o*-dichlorobenzene (*o*-DCB) solution containing the polymer and PC_{70}BM (1 : 3). Finally, 30 nm MoO_3 and 100 nm Ag were deposited by vacuum evaporation at $\sim 2 \times 10^{-7}$ mbar as the back electrode. The device area was 0.1 cm^2.

Double-junction tandem fabrication

LZO and C_{60}-SAM layers were spin-coated on the ITO substrates and annealed at 100 °C for 60 s to form 40 nm and 10 nm layers, respectively. The photosensitive layer of the front subcell was later spin-coated on the LZO/C_{60}-SAM layer. The front subcell PSEHTT:IC_{60}BA was annealed at 100 °C for 1 h. Next, 20 nm pH neutral PEDOT:PSS was spin-coated at 900 rpm for 1 min and baked at 120 °C for 1 min. Later, the ETL comprised of LZO was deposited at 800 rpm for 1 min (and baked at 100 °C for 3 min) on the pH-neutral PEDOT:PSS hole transport layer, at approximately 30 nm. Subsequently, C_{60}-SAM was solution-deposited on the LZO surface at approximately 10 nm. Later, the bottom subcell PTB7:PC_{71}BM was deposited using the previously described procedure and the sample was left idle for 1 h in a glovebox. Finally, a 30 nm MoO_3 layer was thermally evaporated on the bottom subcell, and then 100 nm Ag was deposited through thermal evaporation. The device area was 0.1 cm^2.

Triple-junction tandem fabrication

The LZO and C_{60}-SAM were spin-coated to 40 nm and 10 nm, respectively. Then, the PSEHTT:IC_{60}BA was spin-coated at 650 rpm for 1 min and annealed at 100 °C for 1 h. Later, pH-neutral PEDOT:PSS was spin-coated at 400 rpm for 1 min and baked at 120 °C for 1 min. The LZO layer was then deposited at 450 rpm for 1 min and baked at 100 °C for 3 min. The middle photosensitive materials of PTB7:PC_{71}BM were spin-coated at 800 rpm for 1 min. Afterward, 50 nm of pH-neutral PEDOT:PSS, 50 nm of LZO, and 10 nm of C_{60}-SAM layers were sequentially deposited on the 170 nm PTB7:PC_{71}BM. Next, a 205 nm bottom subcell photosensitive layer PMDPP3T:PC_{70}BM was spin-coated from a mixture of chloroform and *o*-dichlorobenzene (*o*-DCB) solution, followed by thermal evaporation of 30 nm MoO_3. Finally, a 100 nm Ag layer was deposited through thermal evaporation. The device area was 0.1 cm^2. To avoid any degradation, all the single-junction, tandem, and triple-junction PSCs were encapsulated.

Optical and electrical simulations

Computer simulations were performed for the tandem and triple-junction PSCs according to the previously published work.[68] In brief; all single-junction PSCs were evaluated as functions of layer thickness. Subsequently, the internal quantum efficiencies and *J–V* curves as functions of different layer thicknesses were extracted. Optical simulations utilizing the transfer matrix formalism were carried out using commercially available software from Lumerical.[69] Depending on the device layout, the current generated from each subcell was obtained. Combining the current generation and *J–V* shapes, as well as *J–V* for each subcell, the *J–V* curves for all relevant thicknesses were obtained for the tandem and triple-junction PSCs.

Device characterization

For tandem and triple-junction solar cells, the layers comprising LZO/C_{60}-SAM/PSEHTT:IC_{60}BA/pH-neutral PEDOT:PSS/LZO/C_{60}-SAM/PTB7:PC_{71}BM and LZO/C_{60}-SAM/PSEHTT:IC_{60}BA/pH-neutral PEDOT:PSS/LZO/C_{60}-SAM/PTB7:PC_{71}BM/pH-neutral PEDOT:PSS/LZO/C_{60}-SAM/PMDPP3T:PC_{70}BM, respectively, were electrically isolated using toluene and methanol along the perimeter defined by the area of the top electrode. This isolation avoids fringing effects and also prevents an overestimation of the photocurrents generated by the tandem and triple-junction cells. During the measurements and stability tests, a shadow mask (0.1 cm^2) with a single aperture was placed onto the tandem and triple-junction solar cells, in order to define its active area. The current density–voltage (*J–V*) characteristics were recorded with a Keithley 2410 source unit. The EQE measurements were performed using an EQE system (model 74 000) obtained from Newport Oriel Instruments, USA, and an HAMAMATSU calibrated silicon cell photodiode used as a reference diode. The wavelength was controlled with a monochromator 200–1600 nm. The optical parameters *n* and *k* were obtained through spectroscopic ellipsometry.

Acknowledgements

This work was supported by CAPES-PNPD Project no. 3076/2010 and Human Resources Development program (no.

20134010200490) of the Korea Institute of Energy Technology Evaluation and Planning (KETEP) grant funded by the Korea government Ministry of Trade, Industry and Energy.

References

1 G. Yu, J. Gao, J. C. Hummelen, F. Wudl and A. J. Heeger, *Science*, 1995, **270**, 1789.
2 G. Li, R. Zhu and Y. Yang, *Nat. Photonics*, 2012, **6**, 153.
3 L. T. Dou, J. B. You, J. Yang, C. C. Chen, Y. J. He, S. Murase, T. Moriarty, K. Emery, G. Li and Y. Yang, *Nat. Photonics*, 2012, **6**, 180.
4 Z. C. He, C. M. Zhong, S. J. Su, M. Xu, H. B. Wu and Y. Cao, *Nat. Photonics*, 2012, **6**, 591.
5 G. Li, V. Shrotriya, J. S. Huang, Y. Yao, T. Moriarty, K. Emery and Y. Yang, *Nat. Mater.*, 2005, **4**, 864.
6 G. J. Zhao, Y. J. He and Y. F. Li, *Adv. Mater.*, 2010, **22**, 4355.
7 O. Inganas, F. L. Zhang and M. R. Andersson, *Acc. Chem. Res.*, 2009, **42**, 1731.
8 Y. Y. Liang, D. Q. Feng, Y. Wu, S. T. Tsai, G. Li, C. Ray and L. P. J. Yu, *J. Am. Chem. Soc.*, 2009, **131**, 7792.
9 J. C. Bijleveld, V. S. Gevaerts, D. Di Nuzzo, M. Turbiez, S. G. J. Mathijssen, D. M. de Leeuw, M. M. Wienk and R. A. J. Janssen, *Adv. Mater.*, 2010, **22**, E242.
10 J. C. Bijleveld, A. P. Zoombelt, S. G. J. Mathijssen, M. M. Wienk, M. Turbiez, D. M. De Leeuw and R. A. J. Janssen, *J. Am. Chem. Soc.*, 2009, **131**, 16616.
11 C. M. Amb, S. Chen, K. R. Graham, J. Subbiah, C. E. Small, F. So and J. R. Reynolds, *J. Am. Chem. Soc.*, 2011, **133**, 10062.
12 J. W. Jung, F. Liu, T. P. Russell and W. H. Jo, *Energy Environ. Sci.*, 2013, **6**, 3301.
13 K. H. Hendriks, G. H. L. Heintges, V. S. Gevaerts, M. M. Wienk and R. A. J. Janssen, *Angew. Chem., Int. Ed.*, 2013, **52**, 8341.
14 S. Zhang, L. Ye, W. Zhao, D. Liu, H. Yao and J. Hou, *Macromolecules*, 2014, **47**, 4653.
15 L. Ye, S. Zhang, W. Zhao, H. Yao and J. Hou, *Chem. Mater.*, 2014, **26**, 3603.
16 J. Peet, J. Y. Kim, N. E. Coates, W. L. Ma, D. Moses, A. J. Heeger and G. C. Bazan, *Nat. Mater.*, 2007, **6**, 497.
17 W. L. Ma, C. Y. Yang, X. Gong, K. Lee and A. J. Heeger, *Adv. Funct. Mater.*, 2005, **15**, 1617.
18 A. R. B. M. Yusoff, H. P. Kim and J. Jang, *Nanoscale*, 2014, **6**, 1537.
19 H. P. Kim, A. R. B. M. Yusoff, H.-M. Kim, H.-J. Lee, G. J. Seo and J. Jan, *Nanoscale Res. Lett.*, 2014, **1**, 150.
20 S. J. Lee, H. P. Kim, A. R. B. M. Yusoff and J. Jang, *Sol. Energy Mater. Sol. Cells*, 2014, **120**, 238.
21 S. J. Lee, A. R. B. M. Yusoff and J. Jang, *RSC Adv.*, 2014, **4**, 20242.
22 A. R. B. M. Yusoff, H. P. Kim and J. Jang, *Sol. Energy Mater. Sol. Cells*, 2013, **109**, 63.
23 H. P. Kim, A. R. B. M. Yusoff and J. Jang, *Org. Electron.*, 2012, **13**, 3195.
24 A. R. B. M. Yusoff, H. P. Kim and J. Jang, *Org. Electron.*, 2012, **13**, 2379.
25 A. R. B. M. Yusoff, H. P. Kim and J. Jang, *Sol. Energy Mater. Sol. Cells*, 2013, **110**, 87.
26 J. You, L. Dou, K. Yoshimura, T. Kato, K. Ohya, T. Moriarty, K. Emery, C.-C. Chen, J. Gao, G. Li and Y. Yang, *Nat. Commun.*, 2012, **4**, 1446.
27 A. R. B. M. Yusoff, S. J. Lee, F. K. Shneider, W. J. da Silva and J. Jang, *Adv. Energy Mater.*, 2014, DOI: 1002/aenm.201301989.
28 A. R. B. M. Yusoff, S. J. Lee, J.-Y. Kim, F. K. Shneider, W. J. da Silva and J. Jang, *ACS Appl. Mater. Interfaces*, 2014, **6**, 13079.
29 A. R. B. M. Yusoff, S. J. Lee, H. P. Kim, F. K. Shneider, W. J. da Silva and J. Jang, *Adv. Funct. Mater.*, 2014, **24**, 2240.
30 A. R. B. M. Yusoff, W. J. da Silva, H. P. Kim and J. Jang, *Nanoscale*, 2013, **5**, 11051.
31 A. R. B. M. Yusoff, H. P. Kim and J. Jang, *Energ. Tech.*, 2013, **1**, 212.
32 C.-C. Chen, L. Dou, J. Gao, W.-H. Chang, G. Li and Y. Yang, *Energy Environ. Sci.*, 2013, **6**, 2714.
33 Y. Chen, W. –C. Lin, J. Liu and L. M. Dai, *Nano Lett.*, 2014, **14**, 1467.
34 J. Gilot, M. M. Wienk and R. A. J. Janssen, *Adv. Mater.*, 2010, **22**, E67.
35 J. You, C.-C. Chen, Z. Hong, K. Yoshimura, K. Ohya, R. Xu, S. Ye, J. Gao, G. Li and Y. Yang, *Adv. Mater.*, 2013, **25**, 3973.
36 V. C. Tung, J. Kim, L. J. Cote and J. Huang, *J. Am. Chem. Soc.*, 2011, **133**, 9262.
37 http://www.heliatek.com/newscenter/presse/?lang=en.
38 S. Esiner, H. van Eersel, M. M. Wienk and R. A. J. Janssen, *Adv. Mater.*, 2013, **25**, 2932.
39 W. Li, A. Furlan, K. H. Hendriks, M. M. Wienk and R. A. J. Janssen, *J. Am. Chem. Soc.*, 2013, **135**, 5529.
40 X. Che, X. Xiao, J. D. Zimmerman, D. Fan and S. R. Forrest, *Adv. Energy Mater.*, 2014, DOI: 10.1002/aenm.201400568.
41 C.-C. Chen, W.-H. Chang, K. Yoshimura, K. Ohya, J. You, J. Gao, Z. Hong and Y. Yang, *Adv. Mater.*, 2014, **26**, 5670.
42 J. P. Connolly, D. Mencaraglia, C. Renard and D. Bouchier, *Prog. Photovoltaics*, 2014, **22**, 810.
43 H. Xin, S. Subramaniyan, T.-W. Kwon, S. Shoaee, J. R. Durrant and S. A. Jenekhe, *Chem. Mater.*, 2012, **24**, 1995.
44 Y. J. He, H.-Y. Chen, J. H. Hou and Y. F. Li, *J. Am. Chem. Soc.*, 2010, **132**, 1377.
45 Y. Y. Liang, Z. Xu, J. B. Xia, S. T. Tsai, Y. Wu, G. Li, C. Ray and L. P. Yu, *Adv. Mater.*, 2010, **22**, E135.
46 C. P. Chen, S. H. Chan, T. C. Chao, C. Ting and B. T. Ko, *J. Am. Chem. Soc.*, 2008, **130**, 12828.
47 J. Gilot, M. M. Wienk and R. A. J. Janssen, *Adv. Funct. Mater.*, 2010, **20**, 3904.
48 C. J. Brabec, A. Cravino, D. Meissner, N. S. Sariciftci, T. Fromherz, M. T. Rispens, L. Sanchez and J. C. Hummelen, *Adv. Funct. Mater.*, 2001, **11**, 374.
49 A. Gadisa, M. Svensson, M. R. Andersson and O. Inganas, *Appl. Phys. Lett.*, 2004, **84**, 1609.
50 http://arxiv.org/abs/1011.0956.
51 J. U. Lee, J. W. Jung, J. W. Jo and W. H. Jo, *J. Mater. Chem.*, 2012, **22**, 24265.
52 C. H. Peters, I. T. S. Quintana, J. P. Kastrop, S. Beaupre, M. Leclerc and M. D. McGehee, *Adv. Energy Mater.*, 2011, **1**, 491.

53 B. J. Kim, Y. Miyamoto, B. Ma and J. M. J. Frechet, *Adv. Funct. Mater.*, 2009, **19**, 2273.
54 N. Murthy, Y. X. Thng, S. Schuck, M. C. Xu and J. M. J. Frechet, *J. Am. Chem. Soc.*, 2002, **124**, 12398.
55 Y. Sun, C. J. Takacs, S. R. Cowan, J. H. Seo, X. Gong, A. Roy and A. J. Heeger, *Adv. Mater.*, 2011, **23**, 2226.
56 O. Pachoumi, C. Li, Y. Vaynzof, K. K. Banger and H. Sirringhaus, *Adv. Energy Mater.*, 2013, **3**, 1428.
57 T. Hu, F. Li, K. Yuan and Y. Chen, *ACS Appl. Mater. Interfaces*, 2013, **5**, 5763.
58 M. J. Tan, S. Zhong, J. Li, Z. Chen and W. Chen, *ACS Appl. Mater. Interfaces*, 2013, **5**, 4696.
59 G. M. Kim, I. S. Oh, A. N. Lee and S. Y. Oh, *J. Mater. Chem. A*, 2014, **2**, 10131.
60 R. L. Z. Hoye, D. M. Rojas, D. C. Iza, K. P. Musselman and J. L. M. Driscoll, *Sol. Energy Mater. Sol. Cells*, 2013, **116**, 197.
61 A. Pivrikas, N. S. Sariciftci, G. Juska and R. Osterbacka, *Prog. Photovoltaics*, 2007, **15**, 677.
62 M. Lenes, L. J. A. Koster, V. D. Mihailetchi and P. W. M. Blom, *Appl. Phys. Lett.*, 2006, **88**, 243502.
63 L. J. A. Koster, V. D. Mihailetchi and P. W. M. Blom, *Appl. Phys. Lett.*, 2006, **88**, 052104.
64 Y. Yuan, J. Huang and G. Li, *Green*, 2011, **1**, 65.
65 S. Sista, Z. Hong, L. M. Chen and Y. Yang, *Energy Environ. Sci.*, 2011, **4**, 1606.
66 A. Yakimov and S. R. Forrest, *Appl. Phys. Lett.*, 2002, **80**, 1667.
67 S. K. Hau, H. L. Yip, H. Ma and A. K. Y. Jen, *Appl. Phys. Lett.*, 2008, **93**, 233304.
68 K. X. Steirer, P. F. Ndione, N. W. Widjonarko, M. T. Lloyd, J. Meyer, E. L. Ratcliff, A. Kahn, N. R. Armstrong, C. J. Curtis, D. S. Ginley, J. J. Berry and D. C. Olson, *Adv. Energy Mater.*, 2011, **1**, 813.
69 https://www.lumerical.com/.

